Modeling and Measurements of the Radiative Characteristics of High-Power α-DFB Lasers

Katrin Paschke, Alexander Bogatov, Alexander E. Drakin, Reiner Güther, Alexey A. Stratonnikov, Hans Wenzel,
Götz Erbert, *Member, IEEE,* and Günther Tränkle, *Member, IEEE*

***Abstract*—A new above-threshold model of α–DFB lasers is presented. It is based on a generalized beam-propagation method and takes into account spatial hole burning and self-heating effects. Up to moderate output powers, a good agreement between simulated and measured radiative characteristics is obtained. The theoretical model was used to design an optimized laser structure with a 4-mm-long cavity, which yielded a maximum output power of 3 W with a times-diffraction–limit factor of $\mathrm{M}^2 \approx 3$.**

***Index Terms*—distributed feedback laser (α–DFB laser), high brightness, high-power semiconductor laser, modeling, simulation, slanted Bragg grating, spectrum.**

I. INTRODUCTION

HIGH–BRIGHTNESS semiconductor lasers are key elements in emerging technologies such as space and fiber communication, optical frequency conversion, optical radar, and others. The angled-grating distributed-feedback laser (α–DFB laser) [1]–[6] and its generalization, the photonic-crystal distributed-feedback (PCDFB) laser [7], [8] are ideally suited for these applications. The spatial and spectral single-mode high-power emission characteristics of the α-laser is achieved by a mode filtering mechanism due to repeated Bragg reflections at an angled grating. Usually, the slant angle is in the range between 5° and 20°, with respect to the axis normal to the facet. Due to the complicated interplay of slant angle, cavity length, amplitude of the index modulation of the Bragg grating, and parameters of the semiconductor active medium, it is impossible to find the optimum choice of the parameters in order to achieve a high output power and good beam quality with technological variations only. The solution of the parameter optimization problem requires a simulation of the radiative characteristics of α–DFB lasers.

The published theoretical papers [4], [9], [10], [11], do not allow one to solve the optimization problem fully. For example, in [9] and [10], the propagation of the optical radiation in the active region of an α-DFB laser is considered without allowance for the saturation of the gain and spatial hole burning, which is not a good approximation above laser threshold. In [11], a comprehensive simulation of α-DFB lasers operating in the mid-infrared spectral range was presented with account of saturation. However, as in [10], inside the cavity, a coordinate system was employed with one axis parallel to the grooves and the other axis perpendicular to it. In order to satisfy the boundary conditions at the facets, a rotation of the second axis by the slant angle of the grating was performed which led to an oblique coordinate system. Moreover, the anti-index waveguiding action of the injected carriers was taken into account in terms of the linewidth enhancement factor, which is not always a good approximation. From work [11], it remains unclear what is the influence of a lateral waveguide which is formed by a temperature profile due to self-heating. Also, the spectral selectivity of the cavity and the tuning behavior of the lasing wavelength was not clearly determined.

The aim of this paper is to simulate the radiative characteristics of α-DFB lasers emitting in the near-infrared range, with the help of a more realistic physical model which overcomes the above mentioned limitations. The model was applied to design and optimize high-power α-DFB lasers emitting around 1060 nm.

In Section II, the basic equations for the theoretical model and, in Section III, the model for the wavelength determination are presented. The numerical algorithms for the solutions of the model equations are reported in Section IV. In Section V, the fabrication of the α-DFB lasers is described and the theoretical and experimental results are given in Section VI.

II. BASIC EQUATIONS

Fig. 1 illustrates the simulated cavity in the yz plane schematically. The longitudinal z axis lies normal to the laser facets and the lateral y axis parallel to them. L is the cavity length and D is the width of the cavity under study. At the periphery of the cavity, there are two barrier regions with width B, into which spatially chaotic varying refractive indices and absorption coefficients are introduced. Due to these barrier regions, where the outgoing radiation is scattered and absorbed, the influence of the boundary conditions at $y = \pm D/2$ is minimized. In the theoretical model, the range of the Bragg grating is given by $\theta_0(z) \leq y < \theta_1(z)$ and the range of current injection by $y_0(z) \leq y \leq y_1(z)$. The latter means that, in principle, the p-contact can be shaped arbitrarily. In this paper, we assume that all of these functions are given by straight lines with $\theta_0(z), \theta_1(z)$ parallel to the z axis and $y_0(z)$, $y_1(z)$ parallel to the grooves of the grating.

Manuscript received December 23, 2002; revised June 2, 2003. This work was supported by the Deutsche Forschungsgemeinschaft under contract SE 954 /1-2.

K. Paschke, R. Güther, H. Wenzel, G. Erbert and G. Tränkle are with the Ferdinand–Braun–Institut für Höchstfrequenztechnik, 12489 Berlin, Germany (e-mail: paschke@fbh-berlin.de).

A. Bogatov, A. E. Drakin and A. A. Stratonnikov are with the P. N. Lebedev Physical Institute, 119991 Moscow, Russia.

Digital Object Identifier 10.1109/JSTQE.2003.818361

1077-260X/03$17.00 © 2003 IEEE

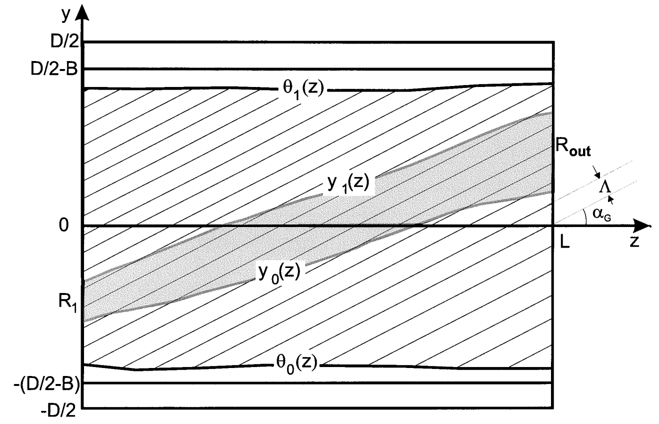

Fig. 1. Schematic top view of an α–DFB laser in the yz plane (L, cavity length; R_1, rear facet reflectivity; R_{out}, output facet reflectivity; Λ, grating period; α_{G}, grating angle; D, total width of cavity; B, width of barrier regions). In the theoretical model, the boundaries of the grating range $\theta_0(z)$ and $\theta_1(z)$ as well as of the electrode stripe $y_0(z)$ and $y_1(z)$ are arbitrary functions.

The grating with period Λ and constant index modulation Δn_{G} is slanted by the angle α_{G} to the z axis. The total dielectric permeability $\varepsilon(y,z)$ of the medium is written as

$$\varepsilon = n_{\mathrm{eff}}^2 + \varepsilon_{\mathrm{G}} + \varepsilon_{\mathrm{M}} \tag{1}$$

where $n_{\mathrm{eff}} = \mathrm{const.}$ is the effective index of the vertical waveguide, ε_{G} describes the built-in Bragg grating and ε_{M} given below in (9) depends on the carrier concentration, the temperature and the fluctuations in the barrier regions. If a grating vector

$$\mathbf{Q} = \frac{2\pi}{\Lambda}(0, \cos\alpha_{\mathrm{G}}, -\sin\alpha_{\mathrm{G}}) \tag{2}$$

is introduced, the part of the permeability describing the grating can be written as

$$\varepsilon_{\mathrm{G}} = n_{\mathrm{eff}}\Delta n_{\mathrm{G}}\left[\mathrm{e}^{i\mathbf{Qr}} + \mathrm{e}^{-i\mathbf{Qr}}\right] \tag{3}$$

with the position vector $\mathbf{r} = (0, y, z)$.

Now, we describe the laser radiation which propagates along the cavity. First, we assume a harmonic time-dependence

$$\mathbf{E}(y,z,t) = \frac{1}{2}\mathbf{E}_\omega(y,z)\mathrm{e}^{-i\omega t} + \mathrm{c.c} \tag{4}$$

where ω is the circular frequency and c.c. denotes complex conjugation. The component $\mathbf{E}_\omega$ fulfills the reduced wave equation

$$\left[\frac{\partial^2}{\partial y^2} + \frac{\partial^2}{\partial z^2} + \frac{\omega^2}{c^2}\varepsilon\right]\mathbf{E}_\omega = 0 \tag{5}$$

where c is the speed of light. Second, after [12] the field is separated into two pairs of forward and backward travelling waves with slowly varying amplitudes u_0^+, u_1^+, u_0^-, u_1^-, namely

$$\begin{aligned}\mathbf{E}_\omega = {} & \mathbf{e}_0 u_0^+(y,z)\mathrm{e}^{ik_0 z} + \mathbf{e}_1 u_1^+(y,z)\mathrm{e}^{i\mathbf{k}_1\mathbf{r}} \\ & + \mathbf{e}_0 u_0^-(y,z)\mathrm{e}^{-ik_0 z} + \mathbf{e}_1 u_1^-(y,z)\mathrm{e}^{-i\mathbf{k}_1\mathbf{r}}\end{aligned} \tag{6}$$

where $k_0 = n_{\mathrm{eff}}\omega/c$, $\mathbf{k}_1 \equiv (0, k_{1y}, k_{1z}) = (0,0,k_0) + \mathbf{Q}$, $\mathbf{e}_0 = (0,1,0)$, and $\mathbf{e}_1 = (0, \cos 2\alpha_{\mathrm{G}}, -\sin 2\alpha_{\mathrm{G}})$. The unit vectors $\mathbf{e}_0$ and $\mathbf{e}_1$, describing the polarization of the electric field, are assumed to lie in the yz plane and to be perpendicular to the respective propagation directions. The former results from the fact that the mode of the vertical waveguide is transverse electric (TE) polarized.

Equations (1), (3), and (6) are now substituted into the wave (5). If terms with equal exponentials $\exp(\pm ik_0 z)$ and $\exp(\pm i\mathbf{k}_1\mathbf{r})$ are compared and terms with higher diffractive orders as well as second order z, derivatives of the slowly varying amplitudes are rejected, two pairs of equations for the coupled waves are obtained which read in operator form

$$\frac{\partial}{\partial z}\begin{bmatrix} u_0^+ \\ u_1^+ \end{bmatrix} = \left(\hat{\mathbf{M}} + \hat{\mathbf{G}} + \hat{\mathbf{D}}^+\right)\begin{bmatrix} u_0^+ \\ u_1^+ \end{bmatrix} \tag{7}$$

and

$$\frac{\partial}{\partial z}\begin{bmatrix} u_0^- \\ u_1^- \end{bmatrix} = -\left(\hat{\mathbf{M}} + \hat{\mathbf{G}} + \hat{\mathbf{D}}^-\right)\begin{bmatrix} u_0^- \\ u_1^- \end{bmatrix} \tag{8}$$

where

$$\begin{aligned}\hat{\mathbf{M}} &= \varepsilon_{\mathrm{M}}\frac{i\omega^2}{2c^2}\begin{bmatrix} \frac{1}{k_0} & 0 \\ 0 & \frac{1}{k_{1z}} \end{bmatrix} \\ \hat{\mathbf{G}} &= \cos(2\alpha_{\mathrm{G}})\Delta n_{\mathrm{G}} n_{\mathrm{eff}}\frac{i\omega^2}{2c^2}\begin{bmatrix} 0 & \frac{1}{k_0} \\ \frac{1}{k_{1z}} & 0 \end{bmatrix}\end{aligned}$$

and

$$\hat{\mathbf{D}}^\pm = \frac{i}{2}\begin{bmatrix} \frac{1}{k_0}\frac{\partial^2}{\partial y^2} & 0 \\ 0 & \frac{1}{k_{1z}}\left[\frac{\partial^2}{\partial y^2} \pm 2ik_{1y}\frac{\partial}{\partial y} + \left(k_0^2 - k_1^2\right)\right] \end{bmatrix}.$$

Here, the operator $\hat{\mathbf{M}}$ is responsible for the action of the semiconductor medium, $\hat{\mathbf{G}}$ for the action of the grating, and $\hat{\mathbf{D}}^\pm$ for the diffraction. The factor $\cos(2\alpha_{\mathrm{G}})$ by which Δn_{G} is multiplied originates from the scalar product $\mathbf{e}_0 \cdot \mathbf{e}_1$ (compare [12, formula (90)]).

Equations (7) and (8) should be supplemented with an expression that determines ε_{M}

$$\varepsilon_{\mathrm{M}} = \varepsilon_N + \varepsilon_{\mathrm{B}} + \varepsilon_T + in_{\mathrm{eff}}\frac{c}{\omega}\alpha_n. \tag{9}$$

Here, ε_N describes the dependence on the carriers, ε_{B} on the fluctuations in the barrier regions, and ε_T on the temperature. The constant coefficient of absorption α_n determines the supplementary losses.

The dependence of ε_N on the carriers is defined as

$$\varepsilon_N = 2n_{\mathrm{a}}\frac{\partial n}{\partial N}N\Gamma - i\frac{c}{\omega}n_{\mathrm{a}}g(N)\Gamma \tag{10}$$

where n_{a} is the active region refractive index, Γ is the active region optical confinement factor, N is a dimensionless concentration defined as $N = N_e/N_0$, N_e is the dimensional (cm^{-3}) concentration of the carriers, and N_0 is the concentration at transparency ($g(N_0) = 0$). The change of the refractive index with carrier concentration is given by the parameter $\partial n/\partial N$ and the material gain is defined as

$$g(N) = \begin{cases} g_0 \ln\left[\frac{N}{(b+cN)}\right], & N > N_{\mathrm{cr}} \\ g_0\left[\frac{1}{2}\left(\frac{N}{N_{\mathrm{cr}}}\right)^2 - 1\right], & 0 \le N < N_{\mathrm{cr}} \end{cases} \tag{11}$$

where g_0, b, and c are parameters fitted on a theoretical gain model [13]. $N_{\mathrm{cr}} = b(\mathrm{e}^{1/2} - c)^{-1}$ is determined such that (11) is a continuous function (for values, see Table I).

TABLE I
VALUES OF THE PARAMETERS INVOLVED IN CALCULATION

parameter	unit	values
L, cavity length	μm	2000 - 4000
w, stripe width	μm	50- 200
D, width of area considered in numerical simulations	μm	1000 - 2000
B, width of damping regions (barriers)	μm	100
$y_0(z)$ and $y_1(z)$, lower and upper bounds of injection area	μm	$y_0(z) = -(w + L \cdot \tan\alpha_G)/2 + \tan\alpha_G \cdot z$ $y_1(z) = (w - L \cdot \tan\alpha_G)/2 + \tan\alpha_G \cdot z$
$\theta_0(z)$ and $\theta_1(z)$, lower and upper bounds of area with a Bragg grating	μm	$\theta_0(z) = -D/2$ $\theta_1(z) = D/2$
λ, vacuum wavelength	μm	1.06
Λ, period of Bragg grating	nm	590 - 885
α_G, slant angle of grating	deg.	10 - 20
$\Delta n_G * \cos(2\alpha_G)$, effective amplitude of the refractive index modulation due to grating		0.002 - 0.004
gain parameters		
g_0	cm^{-1}	1892.2
b		0.96
c		0.0925
N_{cr}		0.62
N_0, transparency concentration (as followed from gain model)	cm^{-3}	$1.058 \cdot 10^{18}$
n_a, refractive index of the active layer		3.6
$\partial n/\partial N$, change of refractive index with carrier density	cm^{-3}	$-1.3 \cdot 10^{-20}$
n_{eff}, effective refractive index		3.45
d_a, thickness of active layer	nm	8
Γ, optical confinement factor for active layer		0.012
n_g, effective group refractive index		4.0
τ, carrier lifetime	ns	2.0
λ_D, diffusion length	μm	1.5
α_n, internal loss	cm^{-1}	1.0
$\partial n/\partial T$, change of refractive index with temperature	K^{-1}	$2 \cdot 10^{-4}$
R_T, specific thermal resistance	K$\cdot$cm$^2\cdot$W^{-1}	0.01 - 0.025
σ_T, mean square length characterizing thermal diffusion	μm	20
σ_1, average conductivity of p doped layers	$(\Omega\text{cm})^{-1}$	4
σ_2, average conductivity of n doped layers	$(\Omega\text{cm})^{-1}$	400
H_1, total thickness of p doped layers	μm	3
H_2, total thickness of n doped layers	μm	100
ΔV, characteristic voltage in thermal model.	V	0.2
R_1, reflection coefficient of rear facet		0.94
R_{out}, reflection coefficient of front facet		0.01
$\delta\alpha_B$, mean-square fluctuation of absorption in the barrier region	cm^{-1}	100
δn_B, mean-square fluctuation of refractive index in the barrier region		0.1

The carrier concentration is determined from the lateral diffusion equation

$$N = \tilde{I} + \left(|u_0^+|^2 + |u_1^+|^2 + |u_0^-|^2 + |u_1^-|^2\right) \times \operatorname{Im} \varepsilon_N(N) + \lambda_D^2 \frac{\partial^2 N}{\partial y^2} \quad (12)$$

where $\varepsilon_N(N)$ is determined in accordance with (10), λ_D is the diffusive length for the carriers, and

$$\tilde{I} = \begin{cases} 0, & y < y_0(z) \\ I, & y_0(z) \le y \le y_1(z) \\ 0, & y > y_1(z). \end{cases} \quad (13)$$

In (13), $I = J/J_0$ is a dimensionless injection current, J is the dimensional injection current, and J_0 is the transparency current

$$J_0 = \frac{N_0 S d_a e}{\tau} \quad (14)$$

where S is the stripe area

$$S = \int_0^L [y_1(z) - y_0(z)]\, dz \quad (15)$$

and d_a is the thickness of the active region, e is the electron charge, and τ is the spontaneous carrier lifetime.

Let us continue the description of the terms in (9). The dielectric constant fluctuation in the barrier regions is defined as

$$\varepsilon_B(y,z) = \begin{cases} 0, & |y| < \frac{D}{2} - B \\ 2n_{eff} n_B \xi + i n_{eff} \alpha_B \frac{c}{\omega} |\eta|, & |y| \ge \frac{D}{2} - B \end{cases} \quad (16)$$

where $n_B \sim 0.1$ and $\alpha_B \sim 100$ cm^{-1} are typical fluctuations of the refractive index and absorption in the barrier regions and $\xi(y,z)$ and $\eta(y,z)$ are two independent δ–correlated random functions with a Gaussian distribution ($M(\xi) = M(\eta) = 0$ and $D(\xi) = D(\eta) = 1$ with M mean and D dispersion).

The value ε_T of (9) is determined from the temperature field $T(y,z)$ as

$$\varepsilon_T = 2n_{eff} \frac{\partial n}{\partial T} \cdot T(y,z) \quad (17)$$

where the constant parameter $\partial n/\partial T$ determines the change of the refractive index with temperature. In our model, the temperature distribution is determined by thermal conduction in the y-direction only and does not depend on the optical field

$$T(y,z) = \frac{R_T J_0 \Delta V}{S} \left(I + \Sigma I^2\right) \frac{1}{\sqrt{2\pi} \cdot \sigma_T} \times \int_{y_0(z)}^{y_1(z)} \exp\left[-\frac{(y-y')^2}{2\sigma_T^2}\right] dy' \quad (18)$$

where R_T is the specific thermal resistivity, σ_T the length of thermal diffusion and ΔV is a characteristic voltage (~ 0.2 V) connected with the thermal relaxation of the carriers. The dimensionless parameter Σ is determined as

$$\Sigma = \frac{J_0}{S\,\Delta V} \left(\frac{H_1}{\sigma_1} + \frac{H_2}{\sigma_2}\right) \quad (19)$$

where H_1 and H_2 are the total thicknesses of p- and n-layers, and σ_1 and σ_2 , respectively, are their average conductivities.

The I-linear term of (18) corresponds to heating due to thermal relaxation of carriers in a heterostructure and the I-squared term corresponds to the Joule heat.

Thus, we have derived the equations which describe the stationary optical field and the carrier concentration inside the cavity under study. To achieve a complete model, we have to supplement it with boundary conditions. As noted above, an introduction of the barrier regions makes the model almost insensitive to the boundary conditions at $y = \pm D/2$. We shall, therefore, use cyclic boundary conditions which are convenient for computations. The conditions at $z = 0$ and $z = L$ are determined by the facet mirrors of the crystal. A strict form of those conditions should contain the term $\exp(2ik_0L)$, which is responsible for the cavity longitudinal mode condition in the model. We shall not take into account that condition because $2k_0L$ is very large ($\sim 10^5$), and the present model does not exhibit such a high spectral selectivity (which is confirmed both by the estimates and the computational experiment).

We can always assume that the longitudinal mode condition is fulfilled for the frequency ω, which is practically the same as that used in the calculation. So we shall not take care for the preserving of the round-trip wave phase $2k_0L$. A stationary solution for the nonlinear problem under study is sought by an iteration method in analogy with the Fox-Li method. By assuming an initial field distribution, $u_0^+(y,0) = u_0^{+(0)}(y,0)$ and $u_1^+(y,0) = u_1^{+(0)}(y,0)$ at $z = 0$, we calculate, by means of (7) and (8), the $u_0^{+(0)}(y,L)$ and $u_1^{+(0)}(y,L)$ at $z = L$ and then reflect the fields to obtain $u_0^{-(0)}(y,L)$ and $u_1^{-(0)}(y,L)$. By returning to $z = 0$ and reflecting the fields $u_0^{-(0)}(y,0)$ and $u_1^{-(0)}(y,0)$, we obtain an initial distribution for the next iteration, $u_0^{+(1)}(y,0)$ and $u_1^{+(1)}(y,0)$. In the same way, the rest of the iterations is performed. The intensities of the counter-propagating fields determined in (7) and (8)–(12) are substituted from the previous iteration. While we solve (7) and (8) for $u_0^{+(n)}$ and $u_1^{+(n)}$, we use the intensity expression in (12) in the form

$$|u_0^{+(n)}|^2 + |u_1^{+(n)}|^2 + |u_0^{-(n-1)}|^2 + |u_1^{-(n-1)}|^2$$

and when we deal with the propagation of $u_0^{-(n)}$, $u_1^{-(n)}$, we use it in the form

$$|u_0^{+(n)}|^2 + |u_1^{+(n)}|^2 + |u_0^{-(n)}|^2 + |u_1^{-(n)}|^2.$$

The other approximation connected with the mirror conditions is the neglection of the waves that arise from reflection of the waves $u_1^+(y,L)$ and $u_1^-(y,0)$, because their wave vectors are far from the diffractive Bragg grating resonance, and they propagate toward the absorbing regions outside the contact stripe and possibly leave the chip at the side walls [9].

Thus, the relations between the fields of $(n-1)$th and nth iterations can be stated as

$$\begin{aligned} u_0^{+(n)}(y,0) &= \sqrt{R_1}\, u_0^{-(n-1)}(y,0) \\ u_1^{+(n)}(y,0) &= 0 \\ u_0^{-(n)}(y,L) &= \sqrt{R_{\text{out}}}\, u_0^{+(n)}(y,L) \\ u_1^{-(n)}(y,L) &= 0 \end{aligned} \tag{20}$$

where R_1 and R_{out} are the intensity reflection coefficients at the facets $z = 0$ and $z = L$. Because the waves $u_1^+(y,L)$ and $u_1^-(y,0)$ are reflected under the angle of total reflection, they do not contribute to the transmitted power, too [see (23)].

The convergence of the iterations (7), (8), and (20) is controlled by the parameters $A^{(n)}$ and $\sigma^{(n)}$ calculated at $z = 0$ from the definitions

$$A^{(n)} = \frac{\int u_0^{+(n)}(y,0)\left[u_0^{+(n-1)}(y,0)\right]^* dy}{\int \left|u_0^{+(n-1)}(y,0)\right|^2 dy} \tag{21}$$

and

$$\sigma^{(n)} = \frac{\int \left|u_0^{+(n)}(y,0) - A^{(n)}\, u_0^{+(n-1)}(y,0)\right|^2 dy}{\int \left|u_0^{+(n)}(y,0)\right|^2 dy} \tag{22}$$

and also by basing on the output power at $z = L$

$$P^{(n)} = P_0(1 - R_{\text{out}}) \int \left|u_0^{+(n)}(y,L)\right|^2 dy \tag{23}$$

with

$$P_0 = \frac{n_{\text{eff}} N_0 \hbar c d_{\text{a}}}{\tau \Gamma}. \tag{24}$$

The iterations are considered to be converging if for $n \leq 50$ the following conditions are fulfilled:

$$\sigma^{(n)} < 10^{-7} \text{ and } \left|P^{(n)} - P^{(n-1)}\right| < 10^{-7} P^{(n-1)}. \tag{25}$$

The convergence controlling parameter (21) can be considered as the amplification factor by which the field amplitude is multiplied after one roundtrip. It will be used for the investigation of the spectral selectivity in the next Section.

III. SPECTRAL SELECTIVITY OF THE α-DFB LASER CAVITY

To a first approximation, the spectral selectivity of the α-DFB laser cavity and the laser wavelength are assumed to be determined by the homogeneous Bragg grating alone. But besides that, spatial variations of ε occur due to self-heating and spatial hole burning effects. This is equivalent to a certain variation of the wave incident angles to the grooves of the Bragg grating. As a result, the spectral properties of the α-DFB laser cavity above threshold differ from those of the "cold" α-DFB laser cavity below threshold.

As will be shown, for simulating the light-current characteristics or for finding the times-diffraction–limit factor M^2 (near and far fields), the laser frequency ω or wavelength λ can be treated as an input parameter. But for the simulation of the spectral characteristics the laser wavelength is to be calculated in a self-consistent way.

To find the lasing wavelength at some injection level, we use an iterative procedure as follows. The total amplification after one round trip is given by $A^{(n)}$. Therefore, we vary firstly λ until the solution of the coupled system of (7), (8), and (12) gives

$$|A(\lambda)| = 1 \tag{26}$$

and using the obtained solution for the carrier concentration, the solution of (7) and (8) for $\lambda \pm \delta\lambda$ gives $|A(\lambda - \delta\lambda)| < 1$ and $|A(\lambda + \delta\lambda)| < 1$. The above relation means that the wavelength λ found corresponds to a spectral maximum of $|A|$.

The "optimal" wavelength λ_{opt}, corresponding to the lasing wavelength, is finally obtained from a parabolic approximation around the maximum of $|A|$ using the wavelengths λ, $\lambda - \delta\lambda$, and $\lambda + \delta\lambda$. Because the amplification of the shorter and longer wavelength waves remains less than unit, single-frequency operation with $\lambda = \lambda_{\text{opt}}$ proves to be stationary. In Section VI, a theoretical blue shift of the emitted light in dependence of the current and an experimental confirmation of this fact will be given.

It should be noted that the above algorithm for finding λ allows us to determine only one local maximum. The calculations have shown that there may be more than one local maximum within the spectral distance $\delta\lambda \approx$ 1–2 nm. Possibly, the wavelength jumps to longer wavelength that happens after a slow shift to shorter wavelength, which is observed experimentally, are due to a jump to another local maximum of $|A(\lambda)|$. Experimental results, shown in Section VI are compatible with this estimation.

Equations (7) and (8) admits a complex value of A, i.e.,

$$A = |A| \cdot \mathrm{e}^{i\varphi}. \tag{27}$$

The term $\exp(i\varphi)$ corresponds to the phase shift at wavelength tuning to an intermode spacing

$$\delta\lambda_m = \frac{\lambda^2}{2Ln_g}. \tag{28}$$

We consider amplification for the modes located from λ by several intermode distances. We, therefore, neglected the phase term $\exp(i\varphi)$ by finding λ. The account of the dependence of φ on λ gives only a numerical correction of the value of $\delta\lambda_m$.

$|A(\lambda)|^2$ has nearly a Lorentzian shape with half-width $\delta\lambda_s$ and with the maximum at the optimal wavelength λ_{opt}. Thus, the half-width $\delta\lambda_s$ which can be approximately obtained from the second derivative of $|A(\lambda)|^2$ at $\lambda = \lambda_{\text{opt}}$

$$\delta\lambda_s = \left(-\frac{d^2|A|^2}{d\lambda^2}\right)^{-1/2} \tag{29}$$

characterizes the spectral selectivity of the cavity, i.e., small values of $\delta\lambda_s$ correspond to a high spectral selectivity.

IV. DESCRIPTION OF THE NUMERICAL MODEL

The functions ε_{B}, ε_T, N, and the random functions ξ and η, used in the numerical model for the field $u^{\pm}_{0,1}(y,z)$, were set on the grid

$$\begin{aligned} y_n &= -\frac{D}{2} + \left(n - \frac{1}{2}\right)\Delta y, \quad n = 0, \ldots, N_y - 1 \\ z_m &= m \cdot \Delta z, \quad m = 0, \ldots, N_z \end{aligned} \tag{30}$$

with

$$\Delta y = \frac{D}{N_y} \qquad \Delta z = \frac{L}{N_z}.$$

The integral (18) for $T(y,z)$ was calculated numerically by a fast Fourier transform (FFT). Equation (13) was approximated by an "interpolation" near to an edge of the stripe. A strict equation for this interpolation can be written in the form

$$\tilde{I}_{nm} = \frac{1}{\Delta y} \int_{y_n - \Delta y/2}^{y_n + \Delta y/2} \tilde{I}(y, z_m) dy. \tag{31}$$

Such a smoothing removes a "stepwise" effect in the stripe profile and, thus, improves the accuracy of the results obtained. This can been observed by studying both the convergence of the numerical model at $N, M \longrightarrow \infty$ and the near field profiles.

The concentration $N(y)$ is obtained from an iterative solution of the nonlinear differential (12) for each z_m. As an initial solution, we used a fixed value $N^{(0)}(y) = N_{\text{cr}}$. In the iterations that follows, $N^{(i+1)}$ is determined as a solution of a linear differential equation

$$\begin{aligned} N^{(i+1)} - \lambda_{\text{D}}^2 \frac{\partial^2 N^{(i)}}{\partial y^2} &= I(y) + F(N^{(i)}) \\ &\quad + F'(N^{(i)}) \left[N^{(i+1)} - N^{(i)}\right] \end{aligned} \tag{32}$$

with the iteration index i.

Here,

$$\begin{aligned} F(N^{(i)}) = \left(| u_0^+ |^2 + | u_1^+ |^2 + | u_0^- |^2 + | u_1^- |^2\right) \\ \times \operatorname{Im} \varepsilon_N(N^{(i)}) \end{aligned} \tag{33}$$

and $F'(N^{(i)})$ is the derivative calculated by the analytical differential of (11). By approximating

$$\frac{\partial^2 N^{(i)}}{\partial y^2} \approx \frac{\left(N^{(i)}_{n+1,m} + N^{(i)}_{n-1,m} - 2N^{(i)}_{n,m}\right)}{(\Delta y)^2} \tag{34}$$

and $\tilde{I}(y)$ in the form of (31) and by superimposing boundary conditions for the absence of a carrier flow at the boundaries of the region under consideration, we obtain a three-diagonal system of equations solved by a sweep method. The iterations $N^{(i)}(y)$ quickly converge (at about six iterations) and take not much of the computer time.

Equations (7) and (8) were solved by a beam propagation method (BPM). One of the quickest variants of that method for the case when $\theta_0(z) = -D/2$, $\theta_1(z) = D/2$ is the one that was described in [11]. The fields $u_0^+(y,z)$ and $u_1^+(y,z)$ are calculated in all layers from $m = 1$ to $m = N_z$ by means of several Fourier transforms of the arrays $u_0^+(y_n, z_m)$ and $u_1^+(y_n, z_m)$ and their component-wise multiplication by the matrices $\exp[\mathbf{M}\Delta z]$ and $\exp[(\mathbf{G} + \mathbf{D}_p^+)\Delta z]$. Here, $\mathbf{D}_p^+$ is the matrix of the $\hat{\mathbf{D}}^+$ operator for the ith Fourier component $p = 2\pi i/D$. In a more general case of $\theta_0(z)$ and $\theta_1(z)$, with the expense of some additional loss of accuracy, the matrices $\exp[(\mathbf{M} + \mathbf{G})\Delta z]$ and $\exp[\mathbf{D}_p^+\Delta z]$ can be used. Equations (7) and (8) for u_0^- and u_1^- were solved in the same way from $m = N_z - 1$ to $m = 0$. The convergence of iterations (14) was determined by $\sigma^{(n)}$ and $P^{(n)}$ in accordance with definitions (22), (23), and (25).

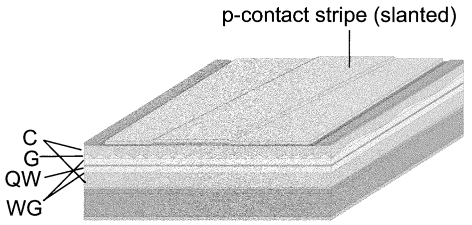

Fig. 2. Schematic of an α–DFB laser. QW: quantum well; WG: waveguide; G: grating; and C: cladding layer.

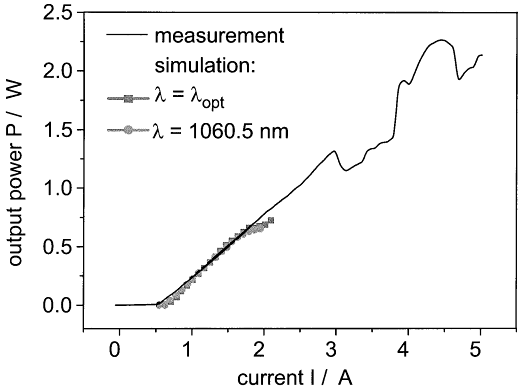

Fig. 3. Theoretical (squares and circles) and experimental (solid line) light-current characteristics of an α–DFB laser with $\alpha_{\mathrm{G}} = 13.5°$, $w = 115\,\mu$m, $\Delta n_{\mathrm{G}}\cos(2\alpha_{\mathrm{G}}) = 0.002\,25$, $R_1 = 94\%$, $R_{\mathrm{out}} = 1\%$, and $L = 2000\,\mu$m. Heat sink temperature $T_{\mathrm{S}} = 25$ °C.

V. FABRICATION OF α-DFB LASERS

For experimental verification, we used α-DFB lasers with a large optical cavity (LOC) structure grown by two-step metal-vapor phase epitaxy (MOVPE). The cavity contains an active InGaAs quantum well with an emission wavelength of 1.06 μm embedded in a GaAs waveguide (0.8-μm-thick) and AlGaAs cladding layers. A scheme of the device is shown in Fig. 2. The Bragg grating was formed on top of the waveguide by stepper lithography and wet-chemical etching. The use of a wafer-stepper had the advantage to allow variations of the grating parameters on the same wafer. We varied the slant angle α_{G} between 10° and 15° (identical for the grating and the contact stripe), the cavity length L between 2 and 4 mm, the stripe width w between 80 μm for $\alpha_{\mathrm{G}} = 10°$ and 160 μm for $\alpha_{\mathrm{G}} = 15°$, and the index modulation Δn_{G}. The facets were coated with high-reflection and low-reflection dielectric layers. Further details of the structure and fabrication process were described in [14]. For the measurements of the radiative characteristics, the devices were soldered p-side down on CuW subcarriers and bonded on copper heatsinks.

VI. THEORETICAL AND EXPERIMENTAL RESULTS

The input values for the simulations are listed in Table I. Fig. 3 shows a measured (solid lines) and simulated (symbols) light-current characteristic of a 2-mm-long α-DFB laser with the following parameters: $w = 115\,\mu$m, $\alpha_{\mathrm{G}} = 13.5°$, $\Delta n_{\mathrm{G}}\cos(2\alpha_{\mathrm{G}}) = 0.002\,25$, $R_1 = 0.94$, and $R_{\mathrm{out}} = 0.01$. The grating period is $\Lambda = 658$ nm corresponding to the Bragg condition

$$\lambda = 2n_{\mathrm{eff}}\Lambda\sin\alpha_{\mathrm{G}} \tag{35}$$

for $\lambda = 1060$ nm.

The measurements were done under quasi-cw-conditions, with a pulse length of 1 ms (repetition frequency: 25 Hz) at room temperature. The simulations were performed for two cases. The squares correspond to a fixed wavelength, while circles are determined by searching the local maximum of $|A(\lambda)|$ as described above in Section III. The difference in the calculated light-current characteristics between both cases is very small. It should be noted, that the exact value of the effective index modulation $\Delta n_{\mathrm{G}}\cos(2\alpha_{\mathrm{G}})$ has been treated as a fitting parameter. Because it depends on the exact etch depth and duty cycle of the grating as well as on the refractive indices of the semiconductor layers, its calculation is connected with some uncertainties.

The correspondence between the theoretical and the experimental curves with respect to threshold current and efficiency is quite good up to 650 mW output power. Above this value, the simulations run into (numerical) instabilities and no longer converge. Experimentally, above an output power of 1.3 W, strong nonlinearities in the light-current characteristic are observed, probably due to appearance of higher order modes. The device shows thermal roll over for $P > 2.5$ W.

The numerical instabilities arising in the simulation of the radiative characteristics seem to be connected with a transition to multiwavelength operation and/or filamentation effects. A numerical solution of (7) and (8) proves to be always stable at sufficiently small injection currents and small intensities. But as the current injection increases and the power achieves some critical value P_c, the iterations (21) and (22) become divergent. In Fig. 3, P_c corresponds to 650 mW. In some cases, the iterations converge again at a higher injection current, and one can find a solution for an output power P, which is greater than P_c. However, the solution for $P > P_c$ is very sensitive to the laser parameters and does not always exist. It was found that a controllable and stable regime of a single-frequency operation with a homogeneous lateral field distribution and an output beam divergence close to the diffraction limit can be observed only for $P < P_c$.

Fig. 4 compares theoretical and experimental lateral far and near field distributions of the laser given above. It should be noted that the far field distributions are depicted versus a relative angle scale. The reason is that we did not calibrate exactly the experimental angle with respect to the cavity axis. The maximum of the theoretical intensity distribution is at $\Theta = 0.013°$. In order to compare the experimental and theoretical far field distributions, the calculated curve is shifted along the angle axis so that both maxima coincide. Taking into account that, the theoretical intensity distributions calculated for an output power of $P = 500$ mW agree well with the corresponding experimental curves (lines). There is a good reproduction of the essential features of the field distributions: The nearly Gaussian shape of the far field with full width at half maximum (FWHM) of 0.25° at $P = 0.50$ W, the nearly Gaussian shape of the

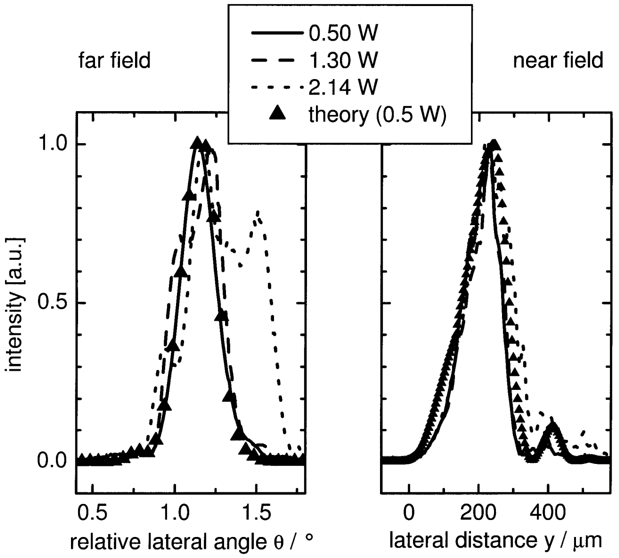

Fig. 4. Theoretical (triangles) and experimental (lines) lateral intensities profiles of (a) far field and (b) near field of the same device as in Fig. 3.

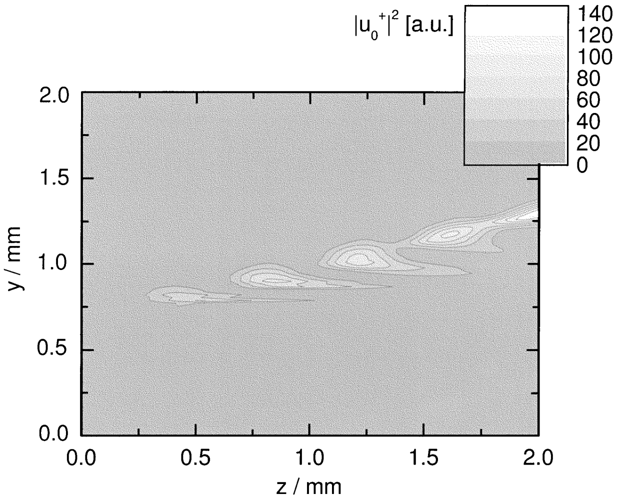

Fig. 5. Contour plot of $|u_0^+(y,z)|^2$ of the same device as in Fig. 4 for $P = 0.5$ W.

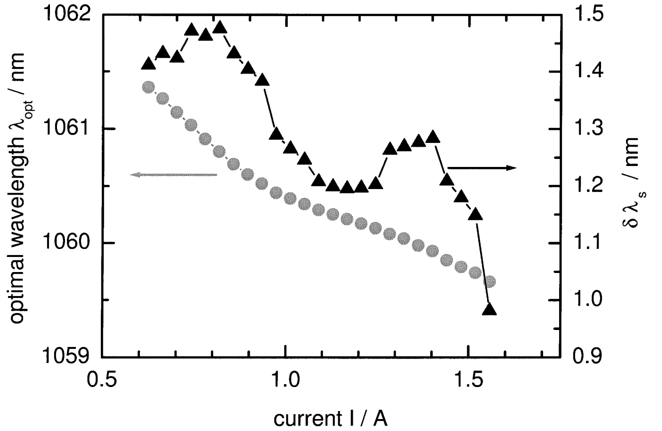

Fig. 6. Calculated optimal wavelength (left axis, circles) and spectral cavity half width (right axis, triangles) versus current.

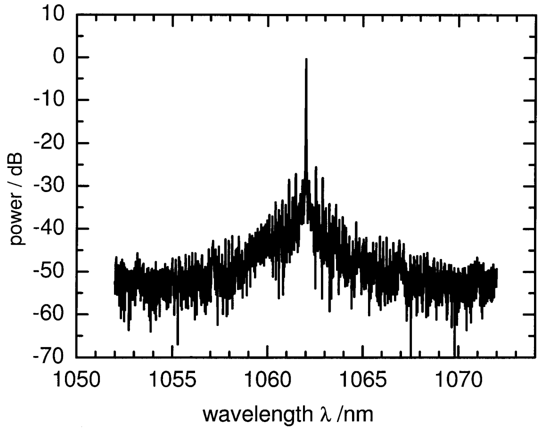

Fig. 7. Optical spectrum of the device of Fig. 3 measured at $P = 2.14$ W.

main lobe of the near field with FWHM of 130 μm and the auxiliary maximum of the near field at $y \approx 400$ μm. Additional measurements of the far and near fields were performed at $P = 1.3$ W and $P = 2.14$ W. Whereas at $P = 1.3$ W, there are only small differences to the field distributions at $P = 0.50$ W, the auxiliary maximum in the near field is clearly larger at $P = 2.14$ W and in the far field a second lobe is visible.

The auxiliary maxima are caused by the limited effectiveness of the Bragg grating. Since the reflection from the facets favors propagation perpendicular to the facets, a part of the radiation travels along a direct path to the facets. This can be clearly seen in the contour plot of the intensity $|u_0^+(y,z)|^2$ in the yz plane (see Fig. 5). Especially at higher output power, this direct path disturbs the light-current characteristic and leads to unwanted side lobes in the near and far field distributions which enhance the times-diffraction–limit factor M^2 (see below). In order to suppress the unwanted lobes, the reflectivity at the output facet was already reduced to $R_{\text{out}} = 0.01$. A further suppression can be achieved by the introduction of highly absorbing regions [15].

The dependence of the calculated optimal laser wavelength λ_{opt} on the current is shown in Fig. 6 (left axis, circles). As the current increases from threshold ($I_{\text{th}} \sim 0.6$ A) to 1.5 A the laser wavelength decreases by more than 1 nm. The second curve (right axis, triangles) represents the value $\delta\lambda_s$ from (29) that characterizes the spectral selectivity of the cavity. It can be seen that $\delta\lambda_s$ decreases by a factor of 1.5 from slightly above threshold to $I = 1.55$ A. This variation corresponds to an increase of the spectral selectivity of the cavity. From that, it can be concluded that a spectral self-stabilization effect is observed under, which subthreshold modes nearby the laser mode suffer increasing losses, both at short and longer wavelengths.

This is the reason for the large side-mode suppression ratio (SMSR) of more than 28 dB obtained experimentally at $P = 2.14$ W to be seen in Fig. 7. The spectral linewidth $\Delta\lambda$ (FWHM) is determined to be smaller than 6 pm. The experimental values for the SMSR and for $\Delta\lambda$ are both limited by the optical spectrum analyzer used (spectral resolution 2 pm).

In order to investigate the spectral behavior in more detail, an experimental mapping of the optical spectrum versus current was performed for a device having the same parameters as that of Fig. 3. The following features are visible in Fig. 8.

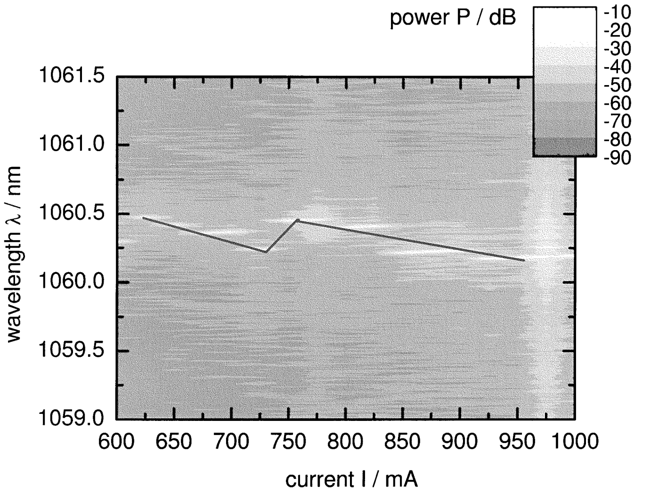

Fig. 8. Gray-scale plot of the optical spectrum versus current of a device having the same parameters as that of Fig. 3. The current step is 25 mA. The solid line indicates the global change of the lasing wavelength.

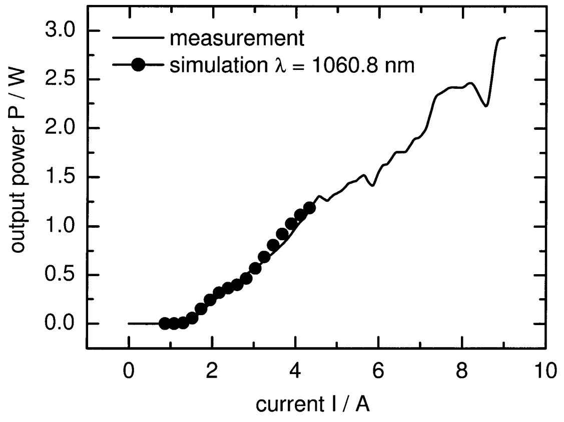

Fig. 9. Theoretical (circles) and experimental (solid line) light-current characteristics of an α–DFB laser with $\alpha_G = 15°$, $w = 160$ μm, $\Delta n_G \cos(2\alpha_G) = 0.003\,12$, $R_1 = 94\%$, $R_{out} = 1\%$, and $L = 4000$ μm. Heat sink temperature: $T_S = 25\,°$C.

If the current is increased, the lasing wavelength remains constant over a current range between 50 and 100 mA before it jumps to the next shorter-wavelength longitudinal mode. At a current of about 750 mA, the lasing wavelength jumps back to a longer-wavelength mode. Above this current, the lasing wavelength shifts again to shorter values. Around $I = 975$ mA, the laser becomes unstable, which can be seen by the broadening of the spectrum. While the shift to shorter wavelengths with increasing current is obtained theoretically, too (cf. Fig. 6), the jump back to longer wavelengths, which is typical for the devices investigated is not yet understood. At some devices, even coexistence of two modes has been observed.

In order to achieve a higher maximum output power, the cavity length was increased from 2 to 4 mm. Fig. 9 shows a measured (solid lines) and simulated (symbols) light-current characteristics of a 4-mm-long α-DFB laser with the following parameters: $\Lambda = 594$ nm, $w = 160$ μm, $\alpha_G = 15°$, $\Delta n_G \cos(2\alpha_G) = 0.003\,12$, $R_1 = 0.94$, and $R_{out} = 0.01$. A maximum output power of 3 W was measured, limited by the electrical current supply.

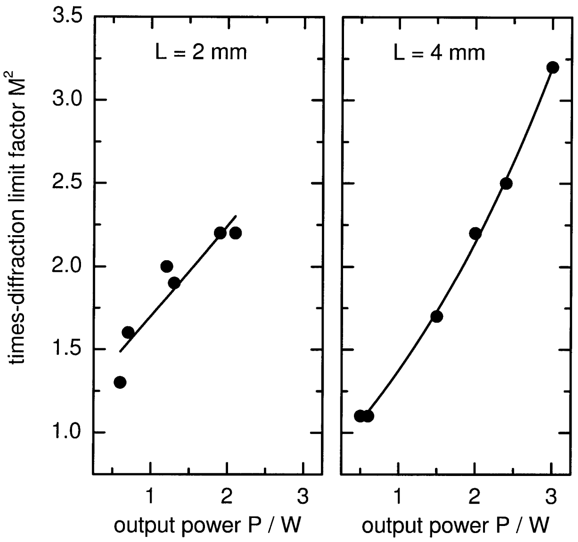

Fig. 10. Measured times-diffraction–limit factor for the devices of Figs. 3 and 9 versus output power. (a) $L = 2$ mm. (b) $L = 4$ mm.

Finally, the times-diffraction limit factor M^2 is depicted for both cavity lengths versus output power in Fig. 10. M^2 was determined from the measured $1/e^2$ widths of the far and near field distributions. For both cavity lengths, $M^2 \approx 2$ at $P = 2$ W and M^2 increases to about 3 at $P = 3$ W for $L = 4$ mm. We should note that despite the kinky experimental light-current characteristics at higher output power, the times-diffraction limit factor is still more than one magnitude smaller than that of an equivalent broad-area Fabry-Perot laser. Thus, the mode selection due to the slanted Bragg grating works very well at high output power, too. The combination of small M^2, high output power, and small spectral linewidth yields a large spectral brightness, which is unique to the α-DFB laser.

VII. CONCLUSION

A new theoretical model for the stationary simulation of α-DFB lasers above threshold was developed and compared to experiments. The optical part includes partial differential equations (first order in z and second order in y) describing four forward and backward propagating main and diffracted waves. These equations are solved numerically by a generalized beam propagation method. The dielectric permeability entering the wave equations depends on the carrier concentration and temperature profiles, which fulfill simplified equations. The simulated light-current characteristics, power-dependent wavelength shift as well as far and near field distributions agree well with the experimentally obtained data up to a power of typically 1 W. Above this value, numerical instabilities are observed. Due to the interplay of simulation, technology and measurement, a 4-mm-long α-DFB laser emitted a record-high output power of 3 W with a times-diffraction–limit factor of $M^2 \approx 3$.

ACKNOWLEDGMENT

The authors thank F. Bugge and J. Fricke, both with FBH Berlin, for the excellent growth and processing of the structures.

REFERENCES

[1] K. M. Dzurko, R. J. Lang, D. F. Welch, D. R. Scifres, and A. Hardy, "650 MW CW single-mode operation of angled grating distributed feedback lasers," *Proc. IEEE/LEOS Annu. Meeting*, vol. 2, pp. 400–401, Nov. 1995.

[2] S. D. DeMars, A. Schönfelder, V. Wong, and R. J. Lang, "Optical properties of angled-grating distributed feedback lasers," *Dig. 16th IEEE Int. Semiconduct. Laser Conf.*, pp. 57–58, Oct. 1998.

[3] V. V. Wong, S. D. DeMars, A. Schönfelder, and R. J. Lang, "Angled–grating distributed feedback laser with 1.2 W cw single–mode diffraction–limited output at 1.06-μm," in *Proc. CLEO*, San Fransisco, CA, May 1998, pp. 34–35.

[4] R. J. Lang, K. Dzurko, A. A. Hardy, S. DeMars, A. Schönfelder, and D. F. Welch, "Theory of grating-confined broad-area lasers," *IEEE J. Quantum Electron.*, vol. 34, pp. 2196–2210, Oct. 1998.

[5] K. Paschke, R. Güther, G. Erbert, J. Sebastian, and H. Wenzel, "Hochleistungshalbleiterlaser mit geneigtem Bragg-Gitter als modenfilter," *Dig. Annu. Meeting DPG*, p. 523, Mar. 2000.

[6] K. Paschke, R. Güther, J. Fricke, J. Sebastian, H. Wenzel, G. Erbert, G. Tränkle, A. P. Bogatov, A. E. Drakin, and A. A. Stratonnikov, "Design, fabrication and characterization of high–power angled–grating distributed–feedback lasers," *Dig. 18th IEEE Int. Semiconduct. Laser Conf.*, pp. 25–26, Oct. 2002.

[7] W. W. Bewley, C. L. Felix, I. Vurgaftman, R. E. Bartolo, J. R. Lindle, J. R. Meyer, H. Lee, and R. U. Martinelli, "Mid-intrared photonic-crystal distributed-feedback laser with enhanced spectral purity and beam quality," *Appl. Phys. Lett.*, vol. 79, pp. 3221–3223, 2001.

[8] I. Vurgaftman and J. R. Meyer, "Photonic-crystal distributed-feedback quantum cascade lasers," *IEEE J. Quantum Electron.*, vol. 38, pp. 592–602, June 2002.

[9] R. Güther, "Beam propagation in an active planar waveguide with an angled Bragg grating (α–laser)," *J. Modern Opt.*, vol. 45, pp. 1537–1546, 1998.

[10] A. M. Sarangan, M. W. Wright, J. R. Marciante, and D. J. Bossert, "Spectral properties of angled-grating high power semiconducter laser," *IEEE J. Quantum Electron.*, vol. 35, pp. 1220–1230, Aug. 1999.

[11] I. Vurgaftman, W. W. Bewley, R. E. Bartolo, C. L. Felix, M. J. Jurkovic, J. R. Meyer, M. J. Yang, H. Lee, and R. U. Martinelli, "Far field characteristics of mid-infrared angled–grating distributed feedback lasers," *J. Appl. Phys.*, vol. 88, pp. 6997–7005, 2000.

[12] H. Kogelnik, "Coupled wave theory for thick hologram gratings," *Bell Syst. Tech. J.*, vol. 48, pp. 2909–2947, 1969.

[13] H. Wenzel, "Gain calculation based on 8×8 kp bandstructure model," Private Communication, 1998.

[14] J. Fricke, M. Matalla, K. Paschke, R. Güther, A. Knauer, F. Bugge, and H. Wenzel, "Fabrication and testing of Bragg gratings for 1060 nm α–DFB lasers," *Proc. SPIE*, vol. 4947, pp. 223–231, 2002.

[15] W. W. Bewley, I. Vurgaftman, R. E. Bartolo, M. J. Jurkovic, C. L. Felix, J. R. Meyer, H. Lee, R. U. Martinelli, G. W. Turner, and M. Manfra, "Limitations to beam quality of mid-IR angled grating distributed feedback lasers," *IEEE J. Select. Topics Quantum Electron.*, pp. 96–101, July 2001.

Katrin Paschke was born in Schwedt, Germany, in 1969. She received the Diploma degree in physics from the University of Potsdam, Potsdam, Germany, in 1996. She is currently pursuing the Ph.D. degree at Ferdinand–Braun–Institut für Höchstfrequenztechnik, Berlin, Germany.

Since 1997, she has been working on noise and reliability of optoelectronical devices at Ferdinand–Braun–Institut für Höchstfrequenztechnik. Her current research interests include modeling and design of the high–power α–DFB laser, as well as device fabrication and characterization.

Alexander Bogatov was born in Suchan, Russia, on September 15, 1947. He received the M.S. degree from the Moscow Institute of Physics and Technology, Moscow, Russia, in 1971, and the candidate's and doctor's degrees in physics and mathematics from the Lebedev Physical Institute, Moscow, Russia, in 1977 and 1996, respectively.

In 1971, he joined the Lebedev Physical Institute, where he is currently the Head of the Injection Laser Laboratory. He is also a Professor at the Moscow Institute of Physics and Technology. His current research interests are in semiconductor lasers, optics, waveguiding and optical nonlinearity, spectral and spatial distributions of optical fields, and intensity fluctuations in injection lasers—theoretical and experimental.

Prof. Bogatov was awarded the State Prize of the USSR in physics in 1984.

Alexander E. Drakin was born in Moscow, Russia, on March 23, 1954. He received the M.S. degree from the Moscow Institute of Physics and Technology, Moscow, Russia, in 1977, and the candidate's degree in physics and mathematics from the Lebedev Physical Institute (LPI), Moscow, Russia, in 1997.

In 1977, he joined the Optoelectronic Department, LPI, where he is now a Senior Researcher. Since joining the LPI, he has been engaged in technology and research of the injection lasers on the base of InGaPAs and InGaAsSb solid solutions. Currently, his research interests include the design and investigation of laser diodes with high brightness.

Reiner Güther received the Diploma degree and the Dr. rer. nat. from the University of Jena, Jena, Germany, in 1964 and 1967 respectively, the Dr. sc. from the Academy of Sciences of Berlin, Berlin, Germany, in 1976, the facultas docendi from the Technical University Ilmenau, Ilmenau, Germany, in 1982, and the Dr. habil. from University Leipzig, Leipzig, Germany, in 1993.

From 1968 to 1991, he was with the Central Institute of Optics and Spectroscopy (ZOS), Berlin of the Academy of Sciences, in part as Department Head for Applied Optics. Since 1992, he has been a Researcher in the Ferdinand-Braun-Institut für Höchstfrequenztechnik, Berlin, Germany. His research activities include quantum field theory, nonlinear optics, volume holography, electro-optics, electromagnetic phenomena and correction theory of holographic concave gratings, diffractive optics, and waveguide coupling, mostly by direct order of optics industry, such as Carl Zeiss or Telekom. His current research activities are the design of semiconductor lasers with planar filtering structures, and laser optics, including micro-optics.

Dr. Güther is a member of DGaO and EOS.

Alexey A. Stratonnikov was born in St. Petersburg, Russia, on December 4, 1977. He received the M.S. degree in 1999 from the Moscow Institute of Physics and Technology, Moscow, Russia, where he is currently pursuing the candidate's degree in physics and mathematics.

His research interests are in the simulation and research of semiconductor lasers.

Hans Wenzel received the Diploma and Doctoral degrees in physics from Humboldt-University, Berlin, Germany, in 1986 and 1991, respectively.

His thesis dealt with the electro-optical modeling of semiconductor lasers. From 1991 to 1994, he was involved in a research project on the three-dimensional simulation of DFB lasers. In 1994, he joined the Ferdinand-Braun–Institut für Höchstfrequenztechnik, Berlin, Germany, where he is engaged in the development of high-power semiconductor lasers. His main research interests include the analysis, modeling, and simulation of optolectronic devices.

Götz Erbert (M'95) received the Diploma in physics from Humboldt-University, Berlin, in 1973 and the Doctoral degree in physics from the Academy of Sciences, German Democratic Republic, in 1990.

From 1973 to 1991, he was with the Academy of Sciences, first on integrated optics and dynamic holographic gratings in semiconductors and later on semiconductor lasers. In 1992, he joined the Ferdinand-Braun-Institut, Berlin, Germany. Since 1996, he has been responsible for the optoelectronic activities in the institute. He is working on high-power semiconductor lasers based on GaAs using strained-layer quantum-well active regions in the wavelength range from 650 to 1200 nm.

Günther Tränkle (M'95) received the Diploma degree in physics from the Technical University (TU), Munich, Germany, in 1981 and the Doctoral degree in physics from the University of Stuttgart, Stuttgart, Germany, in 1988

In 1988, he joined the Walter-Schottky-Institute, TU, where he ran its III/V-semiconductor technology group and worked on field-effect transistors and laser diodes. From 1995 to 1996, he was a Department Head at the Fraunhofer-Institute for Applied Solid-State Physics, Freiburg, Germany, where he was responsible for the development and realization of electronic and optoelectronic III/V semiconductor devices, as well as quantum well infrared detector arrays. In August 1996, he became Head of the Ferdinand-Braun-Institute, Berlin, Germany. Since 2002, he has been Chair of microwaves and optoelectronics at TU. His current research interests include III/V-technology, micro- and mm-wave transistors and circuits, GaN electronics, and high-power diode lasers.